










Article

# Enhanced Direct Dimethyl Ether Synthesis from CO<sub>2</sub>-Rich Syngas with Cu/ZnO/ZrO<sub>2</sub> Catalysts Prepared by Continuous Co-Precipitation

Sabrina Polierer <sup>1</sup>, David Guse <sup>2</sup>, Stefan Wild <sup>1</sup>, Karla Herrera Delgado <sup>1</sup>,  
Thomas N. Otto <sup>1</sup>, Thomas A. Zevaco <sup>1</sup>, Matthias Kind <sup>2</sup>, Jörg Sauer <sup>1</sup>,  
Felix Studt <sup>1,3</sup> and Stephan Pitter <sup>1,\*</sup>

<sup>1</sup> Institute of Catalysis Research and Technology (IKFT), Karlsruhe Institute of Technology (KIT), Hermann-von-Helmholtz-Platz 1, 76344 Eggenstein-Leopoldshafen, Germany; sabrina.polierer@kit.edu (S.P.); stefan.wild@kit.edu (S.W.); karla.herrera@kit.edu (K.H.D.); thomas.otto@kit.edu (T.N.O.); thomas.zevaco@kit.edu (T.A.Z.); J.Sauer@kit.edu (J.S.); felix.studt@kit.edu (F.S.)

<sup>2</sup> Institute of Thermal Process Engineering (TVT), Karlsruhe Institute of Technology (KIT), Kaiserstraße 12, 76131 Karlsruhe, Germany; david.guse@kit.edu (D.G.); matthias.kind@kit.edu (M.K.)

<sup>3</sup> Institute for Chemical Technology and Polymer Chemistry (ITCP), Karlsruhe Institute of Technology (KIT), Kaiserstraße 12, 76131 Karlsruhe, Germany

\* Correspondence: stephan.pitter@kit.edu

Received: 7 July 2020; Accepted: 19 July 2020; Published: 22 July 2020



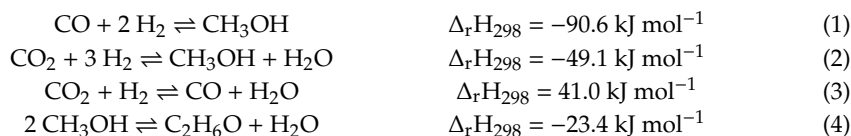
**Abstract:** The manufacturing of technical catalysts generally involves a sequence of different process steps, of which co-precipitation is one of the most important. In this study, we investigate how continuous co-precipitation influences the properties of Cu/ZnO/ZrO<sub>2</sub> (CZZ) catalysts and their application in the direct synthesis of dimethyl ether (DME) from CO<sub>2</sub>/CO/H<sub>2</sub> feeds. We compare material characteristics investigated by means of XRF, XRD, N<sub>2</sub> physisorption, H<sub>2</sub>-TPR, N<sub>2</sub>O-RFC, TEM and EDXS as well as the catalytic properties to those of CZZ catalysts prepared by a semi-batch co-precipitation method. Ultra-fast mixing in continuous co-precipitation results in high BET and copper surface areas as well as in improved metal dispersion. DME synthesis performed in combination with a ferrierite-type co-catalyst shows correspondingly improved productivity for CZZ catalysts prepared by the continuous co-precipitation method, using CO<sub>2</sub>-rich as well as CO-rich syngas feeds. Our continuous co-precipitation approach allows for improved material homogeneity due to faster and more homogeneous solid formation. The so-called “chemical memory” stamped during initial co-precipitation is kept through all process steps and is reflected in the final catalytic properties. Furthermore, our continuous co-precipitation approach may be easily scaled-up to industrial production rates by numbering-up. Hence, we believe that our approach represents a promising contribution to improve catalysts for direct DME synthesis.

**Keywords:** CO<sub>2</sub>-rich syngas; dimethyl ether (DME); methanol (MeOH); copper; zinc; zirconia; co-precipitation; catalyst preparation; catalyst characterization

## 1. Introduction

Power-to-liquid (PtL) processes are promising routes for chemical energy storage and a sustainable mobility based on renewable energies and non-fossil carbon sources like biomass or captured CO<sub>2</sub> [1–3]. In the future, options for combining those processes with the chemical utilisation of CO<sub>2</sub> could gain greater relevance, especially if CO<sub>2</sub> conversion can be efficiently linked to H<sub>2</sub> production from electrolysis processes operated with renewable electrical energy [4]. Besides methanol (MeOH),

dimethyl ether (DME) is one key intermediate in PtL processes [5,6]. Technically, DME can be produced from syngas in a two-step (indirect) process by the separate dehydration of MeOH or in a one-step (direct) process [7]. In the conversion of CO, CO<sub>2</sub> and H<sub>2</sub> to DME, the chemical equilibrium reactions (1) to (4) are relevant.



The direct process requires two admixed catalysts or a bifunctional catalyst system which catalyses both MeOH formation (reactions (1) and (2)) and MeOH dehydration (reaction (4)) [8]. For the hydrogenation of CO<sub>2</sub> to MeOH, the utilisation of ZrO<sub>2</sub>-modified copper catalysts is well established [9–20]. In contrast to the industrially used MeOH catalyst system, Cu/ZnO/Al<sub>2</sub>O<sub>3</sub> (CZA), which is optimised for the selective conversion of CO-rich syngas to MeOH, the Cu/ZnO/ZrO<sub>2</sub> (CZZ) system exhibits a higher tolerance towards water and is therefore favourable for the hydrogenation of CO<sub>2</sub>-rich syngas (reaction (2)) [9]. The exact cause of the promotional effect of ZrO<sub>2</sub> is still vividly debated [14,15,17,21–23]. Among the possibilities being discussed are an enhanced CO<sub>2</sub> adsorption by ZrO<sub>2</sub> [11], and an increased adsorption at the Cu-ZrO<sub>2</sub> interface [14,24] or at copper particles in close contact with the ZrO<sub>2</sub> support [25].

For the preparation of Cu-based catalysts, different synthesis methods have been established, such as conventional batch-wise co-precipitation [26–28], impregnation [29], deposition precipitation [30], or flame spray pyrolysis [18,31]. However, in case of the commonly used co-precipitation, alternative manufacturing approaches have been developed, based on the fundamental knowledge obtained for the key steps of nucleation, crystal growth and ripening, that have the potential for a better control of the material properties, thus paving the way to more efficient catalysts [32–39]. For Cu-based catalysts it is known that the mixing during precipitation strongly influences the initial formation of solids with regard to solid phase distribution and morphology [19,32,34,36,40–42]. In conventional semi-batch operation mode, typically performed in stirred tank type reactors, the spatial and temporally inhomogeneous precipitation conditions such as temperature or reactant concentration can then result in inhomogeneous particle formation [43–45]. To overcome these disadvantages of co-precipitation, Arena et al. [9–11] suggested the reverse co-precipitation under ultrasound irradiation as a novel synthesis route for CZZ methanol catalysts, which yields materials with higher BET surface areas and an increased Cu dispersion. Later on, Haghighi et al. [46,47] studied the effect of both ultrasonic irradiation time and power on the co-precipitation of Cu-based catalysts in more detail. They concluded that the longest and most intense ultrasound irradiation during co-precipitation improves the morphology, particle size, surface area and particle distribution of CZA catalysts compared to non-sonicated samples [47]. However, it is important to stress that a transient mode of operation causes each particle to go through an individual history of solid formation which can further increase the inhomogeneity of the precipitate [48–51]. Therefore, it is essential to prove whether a continuously operated co-precipitation, where mixing limitations should be minimal, gives access to catalysts with an increased degree of homogeneity due to a quasi steady-state, and therefore more homogeneous precipitation conditions [40,52–54].

For MeOH dehydration, solid acid materials such as  $\gamma$ -Al<sub>2</sub>O<sub>3</sub> or selected zeolites are typically used [55–59]. While for direct DME synthesis from CO-rich syngas,  $\gamma$ -Al<sub>2</sub>O<sub>3</sub> is an appropriate and inexpensive dehydration catalyst with a high selectivity towards DME [58], the conversion of CO<sub>2</sub>-rich syngas requires zeolites with enhanced water resistance (reactions (2) and (3)). Recently, ferrierite (FER) type zeolites have been introduced as promising catalysts for this purpose [55,56,60–67].

The aim of our work is to test the practicability of continuous co-precipitation in comparison to conventional semi-batch precipitation for catalysts of the type Cu/ZnO/ZrO<sub>2</sub> (CZZ) used in direct DME synthesis from CO<sub>2</sub>/CO syngas. We base our approach on the assumption that the process parameters of the initial precipitation significantly influence the distribution and the particulate structure of the metal oxide phases present after calcination. In Section 2, we explain and discuss the results of

our investigation, which are based on the experimental and methodological procedures described in Section 3. We have opposed the CZZ materials for comparison with a commercial CZA catalyst (CZA<sup>com</sup>), which is very similar in composition with respect to the metal contents of Cu and Zn.

## 2. Results and Discussion

In initial attempts, we found out that, following the continuous co-precipitation approach, an ageing temperature of 40 °C is probably sufficient to achieve useful catalytic properties of the final catalyst. This aging temperature is lower than for typical semi-batch co-precipitation procedures [42], although Wu et al. [68] suggested that the co-precipitation of Cu-based catalysts should be performed below 40 °C. Therefore, we decided to perform comparative experiments for the co-precipitation of Cu, Zn, and Zr, considering two different ageing temperatures, 60 °C (typical) and 40 °C (reduced).

In our contribution, MeOH catalysts are indicated as CZZ, according to their composition of Cu, Zn and Zr. The superscript indices <sup>BP</sup> for “semi-batch co-precipitation” and <sup>CP</sup> for “continuous co-precipitation” denote the preparation methods. The end numbers, “40” and “60”, represent the respective ageing temperatures. For synthesis of CZZ materials of the “BP”-type, we chose the ultrasonic-assisted variant [9,30]. The influences on the material properties of the calcined pre-catalysts and catalytic efficiency of the reduced catalysts are described in the following sections.

### 2.1. Textural Properties: Metal Composition and N<sub>2</sub> Physisorption

Table 1 summarises the chemical composition of the pre-catalysts, the specific BET surface area ( $S_{\text{BET}}$ ), the cumulative pore volume (PV), the average pore diameters ( $d_{\text{pore, max.}}$ ) and the pore size range ( $d_{\text{pore, range}}$ ).

**Table 1.** Chemical composition, specific surface area ( $S_{\text{BET}}$ ), pore volume (PV) and the maxima and ranges of the pore size distribution ( $d_{\text{pore}}$ ) of the metal oxide pre-catalysts (Cu:Zn:Zr ratio in the precursor solution was 57:29:14 wt%).

Pre-Catalyst	Metal Composition/wt%				$S_{\text{BET}}/\text{m}^2 \text{ g}^{-1}$	PV/cm <sup>3</sup> g <sup>-1</sup>	$d_{\text{pore, max.}}^1/\text{nm}$	$d_{\text{pore, range}}/\text{nm}$
	Cu	Zn	Zr	Al				
CZZ <sup>BP</sup> 40	57	29	14	-	65	0.424	18, 45	20–94
CZZ <sup>BP</sup> 60	57	30	11	-	129	0.448	14	6–22
CZZ <sup>CP</sup> 40	61	31	8	-	125	0.571	14	7–41
CZZ <sup>CP</sup> 60	61	33	5	-	110	0.423	12	6–37
CZA <sup>com</sup>	64	29	-	6	98	0.332	11	5–26

<sup>1</sup> Maximum of the pore size distribution.

The Cu:Zn:Zr metal mass ratios found for the pre-catalysts varied to a certain extent (Cu: 59 ± 2 wt%; Zn: 31 ± 2 wt%; Zr: 9.5 ± 4.5 wt%), although the ratios in all precursor solutions were the same (57:29:14 wt%). For the semi-batch precipitated pre-catalysts CZZ<sup>BP</sup>, this deviation was smaller, whereas for the continuously precipitated CZZ<sup>CP</sup>, a reduced Zr content is noticeable. Additionally, we observe a temperature influence, with the precursors aged at 60 °C (CZZ<sup>BP</sup>60 and CZZ<sup>CP</sup>60) exhibiting considerably lower Zr contents than those aged at 40 °C (CZZ<sup>BP</sup>40 and CZZ<sup>CP</sup>40). The quasi steady-state (continuous) versus the transient (semi-batch) operation mode obviously influences the composition of the final pre-catalyst. Various chemical and rheological aspects have to be taken into consideration to understand the formation of the final materials and bring us to the following hypotheses:

- The different mixing intensities and time-dependencies of semi-batch and continuous co-precipitation results in different rates of phase-specific solid formation in semi-batch and continuous co-precipitation;
- Therefore, the continuous precipitation variant yields a more homogeneous material in terms of phase composition and phase distribution than precipitation in the semi-batch variant;
- Furthermore, the phase composition of the aged product is governed by thermodynamic equilibrium.

Note that for the continuous co-precipitation a reduced overall concentration of the metal nitrate solution was chosen in order to prevent the micromixer from plugging (Section 3.1.2).

The physisorption isotherms of the pre-catalysts are shown in Figure S1 (SI). The specific surface areas ( $S_{\text{BET}}$ ) are summarised in Table 1. Ageing obviously influences surface formation for  $\text{CZZ}^{\text{BP}}$  type pre-catalysts:  $\text{CZZ}^{\text{BP}}40$  exhibits a remarkably small  $S_{\text{BET}}$  of  $65 \text{ m}^2\text{g}^{-1}$ , which is consistent with its less porous characteristics, whereas for  $\text{CZZ}^{\text{BP}}60$  we observe a  $S_{\text{BET}}$  of  $129 \text{ m}^2\text{g}^{-1}$ . A dependency between increasing ageing temperature and  $S_{\text{BET}}$  was also reported by Frei et al. [69], who concluded that  $S_{\text{BET}}$  and pore size distribution are adjustable through the precipitation and ageing temperatures. Our pre-catalysts prepared by continuous co-precipitation generally exhibit large surface areas between  $125$  ( $\text{CZZ}^{\text{CP}}40$ ) and  $110 \text{ m}^2\text{g}^{-1}$  ( $\text{CZZ}^{\text{CP}}60$ ), independent of the applied ageing temperature. The commercial  $\text{CZA}^{\text{com}}$  has a slightly reduced BET surface area with  $98 \text{ m}^2\text{g}^{-1}$ , presumably caused by the stabilisers and/or binders typically present in industrial shaped catalysts.

$\text{CZZ}^{\text{BP}}60$ ,  $\text{CZZ}^{\text{CP}}40$  and  $\text{CZZ}^{\text{CP}}60$  exhibit narrow, gaussian-shaped pore size distributions with pore size maxima of 14, 14 and 12 nm, respectively (Table 1 and Figure 1). The average pore diameters are in the range of 6–22 nm ( $\text{CZZ}^{\text{BP}}60$ ), 7–41 nm ( $\text{CZZ}^{\text{CP}}40$ ) and 6–37 nm ( $\text{CZZ}^{\text{CP}}60$ ), respectively.  $\text{CZA}^{\text{com}}$  exhibits a pore size distribution between 5 and 26 nm, with a maximum at 11 nm. In contrast,  $\text{CZZ}^{\text{BP}}40$  shows a non-uniform, wide pore size distribution shifted to larger pore sizes between 20 and 94 nm, with two maxima at 18 and 45 nm, respectively.

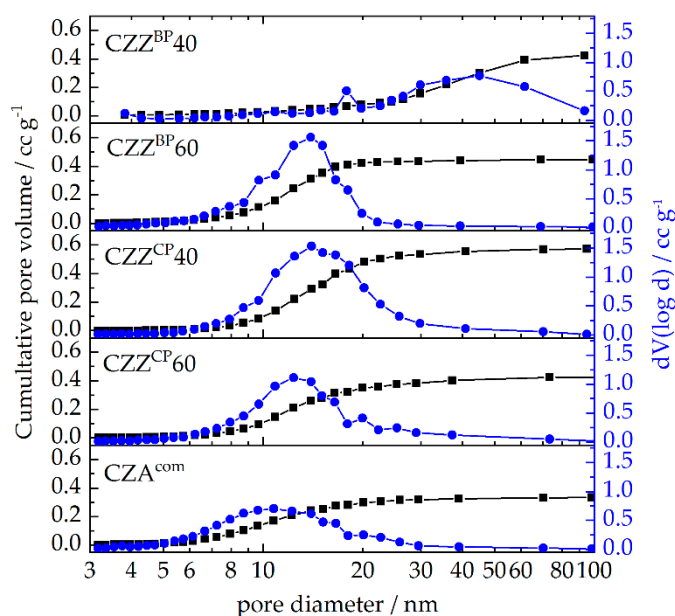


**Figure 1.** Cumulative pore volume and pore size distribution of the calcined CZZ pre-catalysts and  $\text{CZA}^{\text{com}}$  ( $\text{N}_2$  physisorption: 250 g sample, grain size 250–500  $\mu\text{m}$ , pre-treatment: 12 h at 230  $^\circ\text{C}$ ).

Summarising the textural properties, the  $\text{CZZ}^{\text{CP}}$  precursors develop preferential surface properties, less dependent on the ageing temperature. When ageing takes place at 40  $^\circ\text{C}$ , continuous co-precipitation results in more desirable properties than the semi-batch co-precipitation, indicating that intensive mixing during co-precipitation favours important catalytic properties.

## 2.2. Structural Properties: XRD, TEM and EDXS Analyses

The X-ray diffractograms (Figure 2) display the main reflections characteristic for CuO and ZnO surrounded by broad peaks from X-ray amorphous phases. The most intensive reflection for each material at 35.6 $^\circ$  ( $2\theta$ ) results from the overlapping main reflections of ZnO (34.4 and 36.2 $^\circ$  ( $2\theta$ )) and CuO (35.6 $^\circ$  ( $2\theta$ )).  $\text{CZZ}^{\text{BP}}40$  shows slightly sharper main reflections for CuO and ZnO, indicating a larger average particle size. The diffractogram of  $\text{CZZ}^{\text{BP}}60$  exhibits similar features like  $\text{CZZ}^{\text{CP}}40$ , whereas

CZZ<sup>CP</sup>60 shows more intense reflections for ZnO (34.4° (2θ)) and CuO (38.8° (2θ)). Table 2 summarises the estimated CuO crystallite sizes for the five samples calculated from X-ray diffractograms using the Scherrer equation. Noteworthy are the bigger CuO crystallite sizes of about 8 nm for CZZ<sup>BP</sup>40, in comparison to the other pre-catalysts with values ranging between 3 and 4 nm.

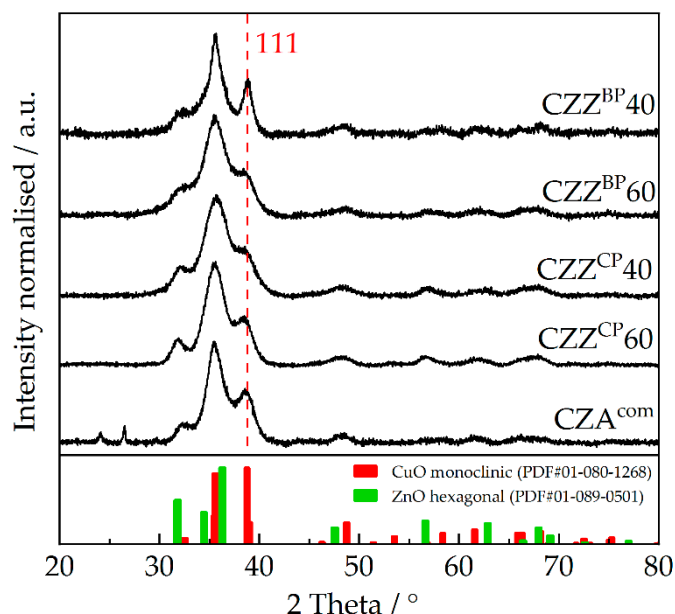


**Figure 2.** X-ray diffraction patterns of the calcined CZZ pre-catalysts and CZA<sup>com</sup> (XRD: 5–80°, 120 min).

**Table 2.** Estimated average CuO crystallite sizes according to Scherrer equation from XRD measurements of the fresh pre-catalysts and the spent catalyst after activity test. Main CuO reflection 2θ received from deconvolution of XRD pattern using Gauss fit.

Catalyst	Fresh Calcined Pre-Catalyst		Spent Catalyst	
	2θ (CuO)/°	d <sub>CuO</sub> /nm	2θ (CuO)/°	d <sub>CuO</sub> /nm
CZZ <sup>BP</sup> 40	38.8	8	38.7	10
CZZ <sup>BP</sup> 60	38.4	3	38.6	10
CZZ <sup>CP</sup> 40	38.6	4	38.6	10
CZZ <sup>CP</sup> 60	38.5	4	38.7	10
CZA <sup>com</sup>	38.5	4	38.8	8

XRD analyses after activity tests in direct DME synthesis (Section 2.4) indicate total re-oxidation of the copper catalysts (Figure S2, SI). CuO particle growth up to 10 nm is found for all CZZ catalysts (Table 2). However, the commercial catalyst CZA<sup>com</sup> is relatively stable against sintering, with a CuO crystallite size of about 8 nm after activity test.

In order to compare the influence of the precipitation methods on the microstructure and distribution of Cu, Zn and Zr on the microscale, TEM measurements for CZZ<sup>BP</sup>40 and CZZ<sup>CP</sup>40 were carried out. Although, according to XRD analyses, a predominantly amorphous material is apparently present (Figure 2), imaging of CZZ<sup>CP</sup>40 in the bright-field TEM (Figure 3A) suggests the presence of crystallite agglomerates smaller than 10 nm in size. In the HAADF-STEM images (Figure 3B,C) CZZ<sup>BP</sup>40 and CZZ<sup>CP</sup>40 show a “cotton wool”-like appearance, which in the case of CZZ<sup>BP</sup>40 seems to be more dense. Diffuse domains in CZZ<sup>BP</sup>40 (Figure 3B) indicate the presence of agglomerate sizes <5 nm, whereas for CZZ<sup>CP</sup>40 (Figure 3C), comparable domains are better resolved and agglomerate sizes of approximately 10 nm are distinguishable. Both samples show domains with an extraordinary, more porous morphology in between these diffuse assemblies of agglomerates, which are more distinct for CZZ<sup>BP</sup>40 (Figure 3B, dashed cycle) and rather small for CZZ<sup>CP</sup>40 (Figure 3C, dashed cycle).



Qualitative EDXS analyses (Figure 4) confirm that these areas with different morphologies mainly contain Zn.

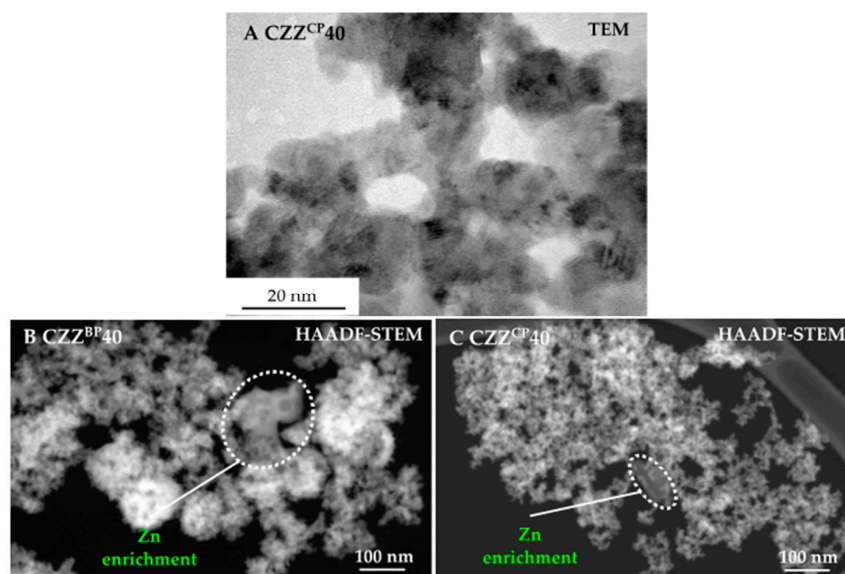


**Figure 3.** TEM image of (A) CZZ<sup>CP</sup>40 of a section of 70 × 80 nm, and HAADF-STEM images of (B) CZZ<sup>BP</sup>40, and (C) CZZ<sup>CP</sup>40 of a section of 1000 × 950 nm.

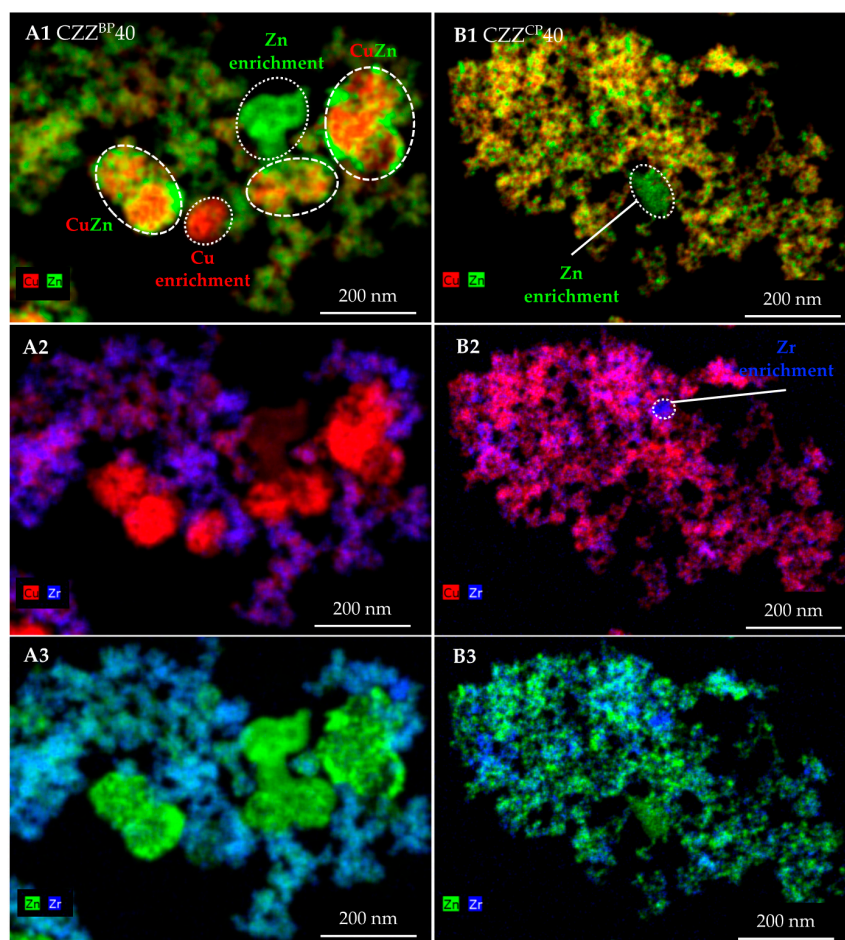


**Figure 4.** EDXS maps of (A) CZZ<sup>BP</sup>40, and (B) CZZ<sup>CP</sup>40. The images show the qualitative distribution of (A1,B1) Cu + Zn, (A2,B2) Cu + Zr, and (A3,B3) Zn + Zr in the pre-catalysts in a section of 630 × 860 nm.

Further, in the EDXS cut-outs of CZZ<sup>BP</sup>40 (Figure 4A1) larger domains exist, consisting of separated CuO- and CuO-ZnO-enriched areas. These domains are poor in ZrO<sub>2</sub>, which is instead distributed in the more homogeneous areas (Figure 4A2,A3). The equivalent domains in CZZ<sup>CP</sup>40 generally look more uniform and we observe a widely homogeneous distribution of CuO, ZnO and ZrO<sub>2</sub> with only few domains of enriched ZnO (Figure 4B1) or ZrO<sub>2</sub> (Figure 4B2), supporting the assumption i (Section 2.1).

In general, the structural characterisation allows for the conclusion that continuous co-precipitation enhances the homogeneity of metal oxides distribution on the particle surface.

### 2.3. Chemisorption Measurements: H<sub>2</sub>-TPR and N<sub>2</sub>O-RFC

Measurements by H<sub>2</sub>-TPR (H<sub>2</sub>-temperature-programmed reduction) and determination of specific copper surface areas S<sub>Cu</sub> by N<sub>2</sub>O-RFC (N<sub>2</sub>O-reactive frontal chromatography) are summarised in Table 3. Complete H<sub>2</sub>-TPR profiles are represented in Figure 5.

**Table 3.** H<sub>2</sub>-TPR and N<sub>2</sub>O-RFC measurements (H<sub>2</sub>-TPR: 5% H<sub>2</sub>/Ar, 1 K min<sup>-1</sup>, RT–300 °C, N<sub>2</sub>O-RFC: 1% N<sub>2</sub>O/He, RT).

Pre-Catalyst	T <sub>red., range</sub> /°C	T <sub>red., max.</sub> /°C	S <sub>Cu</sub> /m <sup>2</sup> g <sup>-1</sup>
CZZ <sup>BP</sup> 40	122–183	157	10
CZZ <sup>BP</sup> 60	113–177	162	25
CZZ <sup>CP</sup> 40	114–174	161	27
CZZ <sup>CP</sup> 60	111–171	159	24
CZA <sup>com</sup>	145–218	181	13

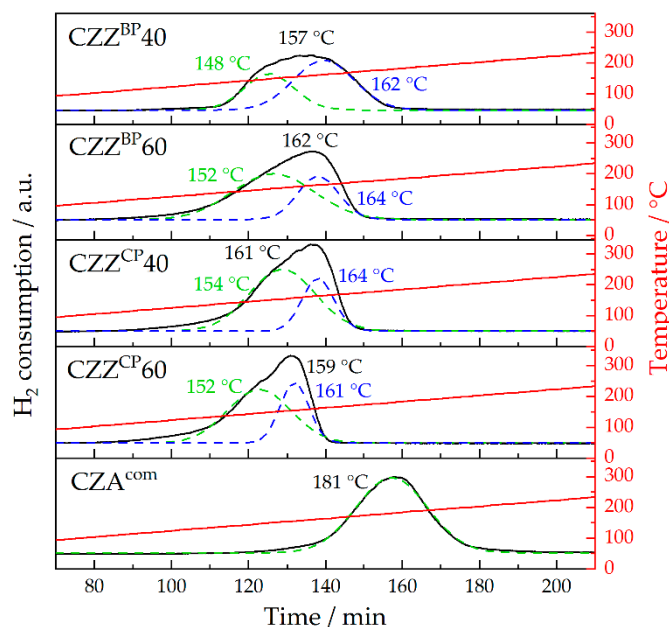


**Figure 5.** H<sub>2</sub>-TPR profiles of the calcined CZZ pre-catalysts and CZA<sup>com</sup> (H<sub>2</sub>-TPR: 5% H<sub>2</sub>/Ar, 1 K min<sup>-1</sup>, RT–300 °C).

Common features of the profiles of the CZZ pre-catalysts are broad signals (for measurement conditions with a width of approximately 50 °C at the applied measurement conditions) and more or less pronounced shoulders at approximately 10 °C below the respective signal maximum. The latter feature indicates the reduction of highly dispersed copper and the main signal is attributed to the reduction of bulk Cu<sup>II</sup>O to Cu<sup>0</sup> [30]. The maxima of the reduction profiles of the CZZ pre-catalysts are in a narrow range between 157 and 162 °C, whereas CZA<sup>com</sup> exhibits a higher reduction maximum of 181 °C. A similar trend was observed by Bonura et al. [62], with a T<sub>red., max.</sub> shift of 13 °C to higher

temperature for a CZA-FER catalyst compared to a CZZ-FER catalyst. For CZZ<sup>BP</sup>40, the reduction branch is shifted by approximately 10 °C to higher temperatures compared to the other CZZ samples. We attribute this to larger CuO particles of about 8 nm for CZZ<sup>BP</sup>40 (Table 2) which are less accessible for reduction compared to smaller particles. Thus, a lower copper dispersion is probable. For CZZ<sup>BP</sup>40, the  $S_{Cu}$  ( $10 \text{ m}^2 \text{ g}^{-1}$ ) is found to be significantly smaller compared to CZZ<sup>BP</sup>60, CZZ<sup>CP</sup>40 and CZZ<sup>CP</sup>60. It is important to note that the semi-batch precipitated CZZ<sup>BP</sup>60, aged at 60 °C exhibits a similar  $S_{Cu}$  to the continuously precipitated samples CZZ<sup>CP</sup>40 and CZZ<sup>CP</sup>60. The commercial methanol catalyst CZA<sup>com</sup>, on the other hand, has a relatively small  $S_{Cu}$  ( $13 \text{ m}^2 \text{ g}^{-1}$ ) compared to the CZZ pre-catalysts.

Summarising the chemisorption measurements, the availability of near-surface copper is obviously directly promoted by the continuous co-precipitation variant. For CZZ materials, these results correlate with the results of the XRD measurements in terms of CuO crystallite size (Section 2.2). Smaller particles usually lead to a larger specific surface area and it is well known from precipitation studies that a higher mixing intensity can lead to smaller particles. This, in turn, supports hypothesis i (Section 2.1).

#### 2.4. Evaluation of the Catalytic Activity and Correlation with Material Properties

Table 4 summarises the productivities to DME ( $P_{DME}$ ) and MeOH ( $P_{MeOH}$ ) as well as the cumulative MeOH productivity ( $P_{MeOH, cum.}$ ) in the conversion of two synthesis gas feeds, CO-rich ( $CO_2/(CO + CO_2) = 0.2$ ) and CO<sub>2</sub>-rich ( $CO_2/(CO + CO_2) = 0.8$ ), respectively. The catalyst bed consisted of the MeOH catalysts, physically mixed with H-FER 20 as a dehydration catalyst. At a reaction temperature of 230 °C and 50 bar, the productivities are generally higher for the CO<sub>2</sub>-rich feed composition compared to the CO-rich composition (Table 4), which agrees with results reported in the literature [70–73]. In preliminary experiments, we observed a decrease in productivity using CO<sub>2</sub>-rich feed at reaction temperatures  $\geq 250$  °C. In this context, we refer to Ruland et al. [70], who studied CO<sub>2</sub> hydrogenation using a commercial CZA catalyst and reported a decrease in the conversion of CO<sub>2</sub>-rich syngas with increasing temperature. A detailed kinetic investigation goes beyond the scope of this work and is focus of an upcoming study.

**Table 4.** Dimethyl ether (DME) ( $P_{DME}$ ), MeOH ( $P_{MeOH}$ ) and cumulative MeOH ( $P_{MeOH, cum.}$ ) productivities of the CZZ catalysts and CZA<sup>com</sup> as physical mixtures of sieve fractions with H-FER 20 (mass ratio 1:1). T = 230 °C, p = 50 bar, modified gas hourly space velocity (GHSV) = 36,000 mL h<sup>-1</sup> g<sup>-1</sup>. The  $P_{MeOH, cum.}$  is calculated according to Equation (S4). Productivities are listed as x/y with x:  $CO_2/(CO + CO_2) = 0.2$  and y:  $CO_2/(CO + CO_2) = 0.8$ . Time on stream (ToS) ranges are given in Table S2 (SI).

Catalyst	$P_{DME}/\text{g h}^{-1} \text{ kg}^{-1}$ (0.2/0.8)	$P_{MeOH}/\text{g h}^{-1} \text{ kg}^{-1}$ (0.2/0.8)	$P_{MeOH, cum.}/\text{g h}^{-1} \text{ kg}^{-1}$ (0.2/0.8)
CZZ <sup>BP</sup> 40/FER	105/129	0/0	146/179
CZZ <sup>BP</sup> 60/FER	240/261	0/42	334/406
CZZ <sup>CP</sup> 40/FER	291/300	9/48	414/465
CZZ <sup>CP</sup> 60/FER	231/247	11/46	332/390
CZA <sup>com</sup> /FER	226/261	0/24	314/387

The maximum productivity  $P_{DME}$  during our tests was  $300 \text{ g h}^{-1} \text{ kg}^{-1}$  using CZZ<sup>CP</sup>40/FER at  $CO_2/(CO + CO_2) = 0.8$ . Putting  $P_{DME}$  and  $P_{MeOH}$  in relation, CZZ<sup>CP</sup>40/FER with 32.2, as expected, offers higher DME selectivity from CO-rich syngas than from CO<sub>2</sub>-rich syngas ( $P_{DME}/P_{MeOH} = 6.3$ ). Besides DME and MeOH, the formation of other organic by-products is largely negligible under these process conditions and is always below the analytical detection limit.

Since the performance difference of CZZ catalysts determines both MeOH and DME formation, we consider the cumulative MeOH productivity  $P_{MeOH, cum.}$  which is defined as the sum of the MeOH converted to DME and the unconverted MeOH (Equation (S1), SI). This is important, as the DME productivity is controlled by the dehydration catalyst as well. The performance results of the



prepared CZZ catalysts were compared with those of the commercial CZA catalyst (CZA<sup>com</sup>). Since we performed all experiments with the same dehydration catalyst, we assume that differences in productivities are attributable to the different copper-based catalysts. Generally, DME and MeOH productivities are higher for the CO<sub>2</sub>-rich feed composition (Table 4) [71–74].

Regarding  $P_{\text{MeOH, cum.}}$ , we conclude that the Cu-based catalysts work efficiently, but the dehydration is limited for active CZZ catalysts due to the correspondingly increased rate of water formation (reactions (2), (3) and (4)), in particular with CO<sub>2</sub>-rich conditions. Catizzone et al. [55] studied the effect of FER zeolite acid sites in MeOH dehydration and confirmed that the presence of Lewis acid sites favours methanol dehydration to DME by lowering barriers to the transition state. However, in the presence of water, the activation enthalpy increases, indicating that water inhibits DME formation. According to the associative mechanism for methanol dehydration proposed by Jones and Iglesia [75], the DME formation rate is affected by the presence of water in the system.

With CZA<sup>com</sup> as the methanol catalyst,  $P_{\text{MeOH, cum.}}$  is reduced by 24% (CO-rich feed) and 17% (CO<sub>2</sub>-rich feed), respectively, compared to the most active CZZ<sup>CP</sup>40. Considering  $P_{\text{MeOH, cum.}}$  (Table 4) the ranking is as follows: CZZ<sup>BP</sup>40 << CZA<sup>com</sup> < CZZ<sup>CP</sup>60 ≤ CZZ<sup>BP</sup>60 << CZZ<sup>CP</sup>40, whereby the differences between CZA<sup>com</sup>, CZZ<sup>CP</sup>60 and CZZ<sup>BP</sup>60 are rather small for CO-rich conditions (<6%). CZZ<sup>BP</sup>40 shows by far the lowest productivity, attributed to reduced  $S_{\text{BET}}$  (65 m<sup>2</sup> g<sup>-1</sup>) and  $S_{\text{Cu}}$  (10 m<sup>2</sup> g<sup>-1</sup>), the presence of larger CuO crystallites (Table 2) and a less homogeneous metal dispersion (Figure 4). CZZ<sup>CP</sup>40 exhibits a significantly higher activity in MeOH formation, and is consequently the highest in DME productivity. Furthermore, CZZ<sup>CP</sup>40 shows a promising long-term stability. After 100 h, ToS CZZ<sup>CP</sup>40 lost 16% of its average activity within 0–5 h ToS, whereas the commercial CZA<sup>com</sup> loses 20% of its average activity.

In general, we conclude that the enhanced homogeneous metal dispersion of CZZ<sup>CP</sup> catalysts enhances the conversion of synthesis gas. Interestingly, the ageing temperature has different effects on the catalytic properties of the products from discontinuous or continuous precipitation. It is known from several publications on semi-batch precipitated copper-based pre-catalysts that ageing temperatures between 60 and 70 °C favour the structuring which is important for catalytic activity (sometimes referred to “chemical memory effect”) [26,27,76,77]. In comparison, the influence of ageing is less apparent with CZZ<sup>CP</sup> materials, indirectly again supporting hypothesis i (Section 2.1). Considerably improved homogeneous distribution of Cu, Zn and Zr already takes place when ageing at 40 °C, which finally results in the most active catalyst. Interestingly, increasing the ageing temperature to 60 °C gives no further improvement and we observe a slightly reduced activity of the final catalyst. In our opinion, on the one hand, this is to be explained by the “chemical memory” of the aged product. On the other hand, for the CZZ<sup>BP</sup> materials, the properties of the aged product are influenced by the ageing temperature, because the ageing time allows for attaining a thermodynamic equilibrium of phase formation, supporting hypothesis iii, stated in Section 2.1. This assumption is strengthened by the observation that the mass fractions of Zr found (Section 2.1) seem to depend more on the ageing temperature than on the precipitation method.

For a more detailed view on potential structure–activity relationships,  $P_{\text{MeOH, cum.}}$  is represented as functions of  $S_{\text{BET}}$  (Figure 6A) and  $S_{\text{Cu}}$  (Figure 6B). Behrens et al. [78] have demonstrated for commercial CZA catalysts that even small amounts of defects are actually responsible for high activities, rather than the entire copper surface area. However, other studies suggest, that the specific Cu surface area  $S_{\text{Cu}}$  in CZA and CZZ catalysts, to some degree correlates, with the catalytic activity in MeOH synthesis [12,79]. Regarding the dependency on  $S_{\text{BET}}$ , some linearity is displayed using CZZ type catalysts, in the conversion of CO<sub>2</sub>-rich (green) as well as of CO-rich (black) syngas (Figure 6A). Linear dependencies between  $P_{\text{MeOH, cum.}}$  and  $S_{\text{Cu}}$  in the series of the CZZ catalysts (Figure 6B) are much more pronounced. Conversely, CZA<sup>com</sup> (triangles, Figure 6B) does not scale with the linear fitting of the CZZ catalysts, as the catalytic activity is high at a relatively low  $S_{\text{Cu}}$  (13 m<sup>2</sup> g<sup>-1</sup>). A similar relationship was found in the work of Kurtz et al. [79], who describe the relationship of activity in MeOH synthesis and  $S_{\text{Cu}}$  as a largely linear relationship, although, according to their findings with optimised preparation

methods, high activities of CZA catalysts are achievable in MeOH synthesis at relatively low  $S_{Cu}$  values. For the use of  $CZA^{com}$  in our study, we assume that industrial manufacturing technologies like the use of additives could also influence the activity. Still, our investigations suggest that  $CZZ^{CP}$  catalysts have particular potential to perform in processes on a similar level to commercial CZA catalysts.

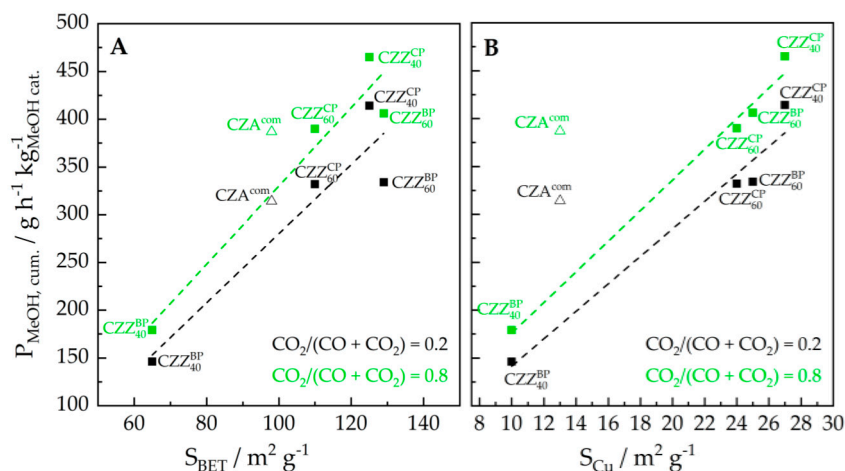


**Figure 6.** Cumulative MeOH productivity  $P_{MeOH, cum.}$  of CZZ/FER and CZA/FER catalysts as a function of (A) the specific BET surface area  $S_{BET}$  and (B) the specific copper surface area  $S_{Cu}$ .  $CZA^{com}$  was not considered in linear fitting. Conditions productivity tests:  $CO_2/(CO + CO_2) = 0.2$  (black) ( $H_2:CO:CO_2:N_2:Ar = 37.5:12.3:15:32.5$  vol%) and 0.8 (green) ( $H_2:CO:CO_2:N_2:Ar = 46.5:3:12:15:23.5$  vol%), 230 °C, 50 bar, GHSV = 36,000  $mL\ h^{-1}\ g^{-1}$ .

### 3. Materials and Methods

#### 3.1. Catalyst Preparation

The syntheses of  $CZZ^{BP}40$ ,  $CZZ^{BP}60$ ,  $CZZ^{CP}40$  and  $CZZ^{CP}60$ , each starting from precursor solutions with a Cu:Zn:Zr ratio of 60:30:10 mol%, corresponding to 57:29:14 wt%, are described in the following sections.

##### 3.1.1. Semi-Batch Co-Precipitation

$CZZ^{BP}40$  and  $CZZ^{BP}60$  were prepared by reverse semi-batch co-precipitation under ultrasonic irradiation following the procedure described by Arena et al. [9] and Frusteri et al. [9,30]. The precursor solutions were prepared by dissolving 11.60 g (0.048 mol) of copper(II) nitrate trihydrate ( $Cu(NO_3)_2 \cdot 3H_2O$ , Merck, Darmstadt, Germany, 99.5%), 7.14 g (0.024 mol) of zinc nitrate hexahydrate ( $Zn(NO_3)_2 \cdot 6H_2O$ , Alfa Aesar, Thermo Fischer, Kandel, Germany, 99%) and 2.71 g (0.008 mol) of zirconium(IV) oxynitrate hexahydrate  $ZrO(NO_3)_2 \cdot 6H_2O$ , Sigma-Aldrich/Merck, Darmstadt, Germany, 99%) in 100 mL of distilled water., followed by stirring at room temperature for 16 h. The solution was then transferred (peristaltic pump: Minipuls 2, Gilson) with a flow rate of 1.6  $mL\ min^{-1}$  into a 2000 mL three-necked flask equipped with mechanical stirrer and pH sensor, containing 1000 mL of a preheated (40 and 60 °C, respectively)  $NaHCO_3$  solution (0.2  $mol\ L^{-1}$ ). The addition of the precursor solution occurs under vigorous stirring, using a standard anchor impeller operated at 520 rpm and under continuous ultrasonic irradiation performed in a lab-scale ultrasonic cleaning bath (Bandelin Sonorex RK 510 H, 35 kHz, 640 W). During the precipitation procedure, the pH was continuously monitored and adjusted between 7.0 and 7.2 by dropwise adding a 1  $mol\ L^{-1}$   $NaHCO_3$  solution. Following the known procedure [9,30], the resulting suspension was then aged for 2 h at 40 °C ( $CZZ^{BP}40$ ) and 60 °C ( $CZZ^{BP}60$ ), respectively, by unchanged stirring and ultrasonic irradiation. Following the ageing period, the suspension was sedimented using a centrifuge (Biofuge Stratos, Thermo Scientific™, Schwerte, Germany, 10,000  $min^{-1}$ ) and the solid residue was washed with distilled water until no more soluble

nitrate could be detected using nitrate test strips (MQuant<sup>TM</sup>, Merck, Germany). The solid was dried for 16 h at 110 °C, finely ground and calcined in air at 350 °C with a heating ramp of 3 K min<sup>-1</sup> for 4 h resulting in 6 g of CZZ metal oxide pre-catalyst.

### 3.1.2. Continuous Co-Precipitation

CZZ<sup>CP</sup>40 and CZZ<sup>CP</sup>60 were prepared by continuous co-precipitation using a setup with a confined impinging micro jet mixer (Y-mixer) (Figure 7), to enable both high volume flow and high energy dissipation rate, as the initial solid formation also proceeds at high precipitation rates. The geometric dimensions of the mixer are given elsewhere [52,53,80,81]. The precursor solutions were prepared by dissolving 29.35 g (0.12 mol) copper(II) nitrate trihydrate (Cu(NO<sub>3</sub>)<sub>2</sub>·3H<sub>2</sub>O, Merck, Darmstadt, Germany, 99.5%), 18.07 g (0.06 mol) zinc nitrate hexahydrate (Zn(NO<sub>3</sub>)<sub>2</sub>·6H<sub>2</sub>O, Alfa Aesar, Thermo Fischer, Kandel, Germany, 99%) and 6.87 g (0.02 mol) zirconium(IV) oxynitrate hydrate (ZrO(NO<sub>3</sub>)<sub>2</sub>·6H<sub>2</sub>O, Sigma-Aldrich/Merck, Darmstadt, Germany, 99%) in 750 mL of distilled water. For the precipitation procedure, 150 mL of the precursor solution and 150 mL of a 1.01 mol L<sup>-1</sup> NaHCO<sub>3</sub> were transmitted simultaneously passed through the mixing unit each with a flow rate of 150 mL min<sup>-1</sup> at ambient temperature (Figure 7). The pH value at the outlet of the mixer was 6.9. The procedure was repeated five times within 10 min, yielding 1500 mL of a light blue suspension in total. The suspension was transferred directly to a double-jacketed 2000 mL glass vessel and aged for 2 h at 40 °C (CZZ<sup>CP</sup>40) and 60 °C (CZZ<sup>CP</sup>60), respectively, under stirring (700 rpm) using a magnetic stirrer. When ageing took place at 60 °C, a characteristic colour change from light blue to cyan was observed after approximately 30 min, indicating the transformation of zincian georgeite to zincian aurichalcite and zincian malachite [82]. The subsequent operations of washing, drying and calcination were analogous to the procedure described for semi-batch co-precipitation (Section 3.1.1), yielding 10 g of the CZZ metal oxide pre-catalyst.

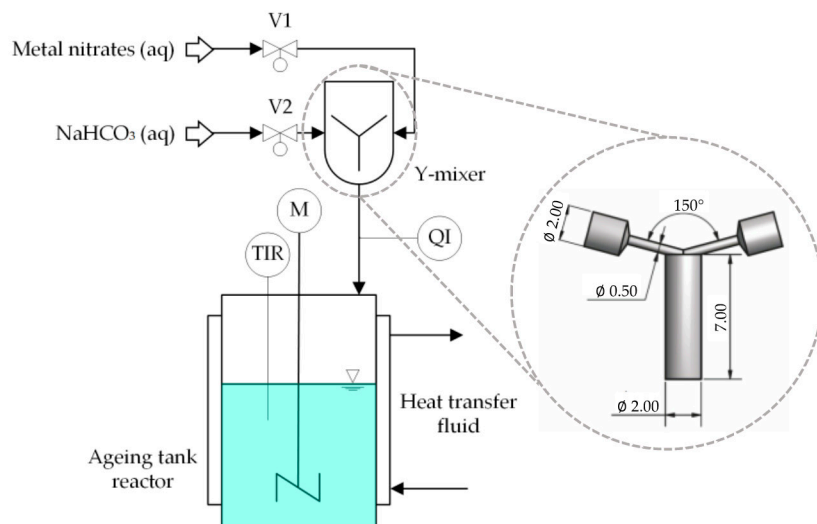


**Figure 7.** Schematic set-up of the continuous co-precipitation (TIR—temperature display and registration, M—motor, QI—pH display) and the dimension of the Y-mixer in mm adapted from [53].

## 3.2. Catalyst Characterisation

### 3.2.1. X-Ray Fluorescence (XRF)

Cu, Zn and Zr contents of the calcined pre-catalysts were determined by X-ray fluorescence analysis (XRF) using a Bruker AXS (Bruker AXS GmbH, Karlsruhe, Germany) wavelength-dispersive S4 Pioneer spectrometer. The samples were measured as finely ground homogeneous powders in plastic sample cups sealed with a 3.5 µm Mylar support film, using an aperture slit of 34 mm and a

tube voltage of 60 kV for the measurement. Data were processed and finalized using the proprietary software SpectraPlus (Eval 17, V 1.7.408, © 2004, 2010, Bruker AXS).

### 3.2.2. X-Ray Diffraction (XRD)

X-ray diffractograms were measured using a Panalytical X'Pert Pro X-ray diffractometer (Malvern Panalytical GmbH, Kassel, Germany) with Bragg-Brentano geometry and Cu K $\alpha$  radiation with a Ni filter. The diffractograms were recorded in the range 5–80° over a period of 120 min. The reflections were evaluated using the HighScore Plus software (version 2.2.e (2.2.5)) and compared to references from the Joint Committee of Powder Diffraction Standards (JCPDS) database. The CuO particle size  $d_{\text{CuO}}$  was calculated based on the CuO reflection at 38.7° (2 $\theta$ ) using the Scherrer equation. For this purpose, broadened main reflections were deconvoluted using gaussian fit.

### 3.2.3. Transmission Electron Microscopy (TEM) and Energy Dispersive X-Ray Spectroscopy (EDXS)

High-angle annular dark-field scanning transmission electron microscopy (HAADF-STEM) imaging combined with energy-dispersive X-ray spectroscopy (EDXS) was used for semi-quantitative analysis of the chemical composition and the metal dispersion on the nanometre scale. For characterisation a FEI Osiris ChemiSTEM microscope operated at 200 keV, equipped with a Bruker Quantax system (XFlash detector) for EDXS measurements was used. TEM sample preparation was performed by mixing the CZZ powders with ultra-pure water and dispensing one droplet of the solution onto a TEM grid using an ultrasonic nebuliser.

### 3.2.4. N<sub>2</sub> Physisorption

N<sub>2</sub> physisorption measurements [83] were carried out on Quantachrome NOVA 2000e and NOVA 3200e devices (Anton Paar GmbH, Graz, Austria) at 77 K. Samples (250 mg, grain size 250–500  $\mu\text{m}$ ) were degassed for 12 h at 230 °C. Isotherms were evaluated with the Brunauer–Emmett–Teller (BET) [84] model in the range of 0.05–0.1 p/p<sub>0</sub>. The pore size distributions were calculated according to the Barret–Joyner–Halenda (BJH) method using the desorption branch of the isotherm [85].

### 3.2.5. H<sub>2</sub> Temperature Programmed Reduction (H<sub>2</sub>-TPR)

H<sub>2</sub> temperature-programmed reduction (H<sub>2</sub>-TPR) was measured at Rubokat GmbH (Ruhr-University of Bochum, Germany). The measurements were carried out in a stainless-steel U-tube reactor without pre-treatment of the samples. Therefore, 100 mg of the calcined CZZ sample (250–500  $\mu\text{m}$ ) was heated in a 5% H<sub>2</sub> in Ar atmosphere to 300 °C with a heating ramp ( $\beta$ ) of 1 K min<sup>-1</sup>. The H<sub>2</sub> uptake was recorded using a thermal conductivity detector (TCD).

### 3.2.6. N<sub>2</sub>O Reactive Frontal Chromatography (N<sub>2</sub>O-RFC)

For estimation of the specific copper surface area ( $S_{\text{Cu}}$ ), N<sub>2</sub>O-RFC was carried out subsequent to the H<sub>2</sub>-TPR measurement with 1% N<sub>2</sub>O in He at ambient temperature. Gas flows were analysed by an Advance Optima 2020 continuous gas analyser (ABB Asea Brown Boveri Ltd., Zurich, Switzerland). The specific copper surface was calculated by integration of the N<sub>2</sub>O signal area. For calculation half monolayer oxygen coverage (stoichiometry of Cu<sub>s</sub>:O<sub>ads</sub> = 2:1) and a mean copper surface atom density of  $1.47 \times 10^{19} \text{ m}^{-2}$  were assumed [86].

## 3.3. Catalyst Performance in Direct DME Synthesis

Direct DME synthesis was performed using a physical mixture of CZZ pre-catalysts and a commercial ferrierite type zeolite (Zeolyst International, Amsterdam, Netherlands, CP914C, Si/Al ratio of 20) as a dehydration catalyst (FER). The zeolite was calcined at 550 °C for 4 h prior to use. CZZ pre-catalysts and FER were separately pressed and sieved into sieve fractions of 250–500  $\mu\text{m}$  particle size and then mixed in equal proportions. To minimise hot spot formation and potential sintering,

CZZ/FER (mass ratio 1:1) was mixed with SiC (Mineraliengrosshandel Hausen GmbH, Telfs, Austria) in a mass ratio of 1:5. Lab-scale DME synthesis was performed in a continuous-flow, stainless-steel fixed bed reactor (460 mm length, 12 mm inner diameter) which was filled with 12 g of the CZZ/FER/SiC mixture. The temperature was measured at the outside of the reactor wall. Prior to the experiments, the catalyst was heated to 100 °C in Ar for 1 h. Catalyst reduction was performed by heating to 200 °C in 5% H<sub>2</sub>/95% Ar with a heating rate of 0.33 K min<sup>-1</sup>, followed first by increasing the H<sub>2</sub> content to 50% and then the temperature to 240 °C with a heating rate of 0.2 K min<sup>-1</sup>. These conditions were kept constant for 5 h. Every catalyst was tested at 230 °C and 50 bar with two feed gas compositions differing in the CO<sub>2</sub>/(CO + CO<sub>2</sub>) ratio (0.2 and 0.8). The modified gas hourly velocity (GHSV) value of 36,000 mL g<sup>-1</sup> h<sup>-1</sup> is related to the mass fraction of the CZZ or CZA catalyst and was chosen to ensure that conversion takes place in the kinetic region. Details on feed compositions and data recording during time on stream (ToS) are provided in Tables S1 and S2. Analysis at the reactor outlet took place by chromatography (Agilent G1530A (Agilent Technologies Germany GmbH & Co. KG, Waldbronn, Germany), equipped with a thermal conductivity (TCD) and flame ionization detector (FID) which were connected to a RT<sup>®</sup>-Msieve 5A column and RT<sup>®</sup>-U-BOND columns). An FTIR spectrometer CX4000 (Gaset Technologies Oy, Vantaa, Finland) was used to determine the water amount. Prior to the experiments using CZA<sup>com</sup>, the commercial material was powdered, pressed and sieved into the proper particle size range of 250–500 µm.

#### 4. Conclusions

Our study was directed to the investigation of two different approaches for co-precipitation-based synthesis of Cu/ZnO/ZrO<sub>2</sub> (CZZ) catalysts. Our results clearly show that well-mixed, quasi steady-state continuous co-precipitation is a promising approach. The spatial homogeneity and temporal quasi-steady state of the initial precipitation, which was present in our Y-jet mixer at high flow rates, result in material properties that are beneficial for later use in catalysis. In accordance with earlier studies, continuous co-precipitation results in changed requirements for subsequent ageing. In our study, 40 °C is a reasonable ageing temperature, whereas a more detailed investigation of the temperature dependencies will certainly offer further optimisation potential. Our results support the hypotheses that, compared to batch precipitation, our continuous precipitation variant increases the homogeneity of the materials. Hence, we conclude that the phase-specific solid formation is kinetically controlled. Yet, with our results for semi-batch co-precipitation, we prove that the phase composition of the aged product is controlled by thermodynamic equilibrium.

The effectiveness of the catalysts in the hydrogenation of CO<sub>2</sub>/CO mixtures coupled with dehydration of the formed methanol (MeOH) to dimethyl ether (DME) is supported by high particle surface areas and good accessibility of the active Cu centres. For catalyst manufacturing technology in general, continuous co-precipitation procedure should allow for straightforward scaling-up to production scale by numbering-up (parallelisation of mixing units). This would enable a high degree of control over material properties to be maintained. Furthermore, it is important to differentiate the precipitation kinetics from mixing influences and to characterise the exact phase composition of the precipitated solids in further investigations. Both scaling-up and fundamental investigations are currently studied by the authors.

**Supplementary Materials:** The following data are available online at <http://www.mdpi.com/2073-4344/10/8/816/s1>, Figure S1: N<sub>2</sub> physisorption isotherms of the calcined CZZ pre-catalysts and CZA<sup>com</sup>. Figure S2: X-ray diffraction patterns of the spent CZZ and CZA<sup>com</sup> catalysts. Table S1: Feed compositions., Table S2: Time on stream (ToS) ranges in which the inlet feeds (Table S1) were measured. Equations (S1)–(S4): Calculation for DME and MeOH productivities.

**Author Contributions:** Conceptualization, S.P. (Sabrina Polierer) and S.P. (Stephan Pitter); methodology, S.P. (Sabrina Polierer) and D.G.; catalyst characterisation, S.P. (Sabrina Polierer), T.N.O.; validation, S.P. (Sabrina Polierer) and S.W.; formal analysis, S.P. (Sabrina Polierer) and K.H.D.; investigation, S.P. (Sabrina Polierer), S.W. and D.G.; resources, J.S. and M.K.; data curation, S.P. (Sabrina Polierer) and S.W.; writing—original draft preparation, S.P. (Sabrina Polierer); writing—review and editing, S.P. (Stephan Pitter) and T.A.Z.; visualization, S.P. (Sabrina Polierer);



supervision, J.S., F.S. and M.K.; project administration, S.P. (Stephan Pitter); funding acquisition, J.S. All authors have read and agreed to the published version of the manuscript.

**Funding:** This research was funded by from the Helmholtz Association, Research Programme “Storage and Cross-linked Infrastructures”, Topic “Synthetic Hydrocarbons”.

**Acknowledgments:** We kindly acknowledge the Chair of Industrial Chemistry at Ruhr-University Bochum for H<sub>2</sub>-TPR and N<sub>2</sub>O-RFC measurements (Volker Hagen, Noushin Arshadi, Sascha Stürmer and Martin Muhler), the Laboratory for Electron Microscopy at Karlsruhe Institute of Technology for TEM-EDXS measurements (Heike Störmer and Radian Popescu) and Zeolyst International for providing H-FER 20 zeolite. Furthermore, we acknowledge support by the KIT-Publication Fund of the Karlsruhe Institute of Technology.

**Conflicts of Interest:** The authors declare no conflict of interest.

## References

1. Henrich, E.; Dahmen, N.; Dinjus, E.; Sauer, J. The role of biomass in a future world without fossil fuels. *Chem. Ing. Tech.* **2015**, *87*, 1667–1685. [[CrossRef](#)]
2. Arshadi, M.; Sellstedt, A. Biomass-based energy production. In *Introduction to Chemicals from Biomass*, 2nd ed.; Clark, J., Deswarte, F., Eds.; John Wiley & Sons: Hoboken, NJ, USA, 2015; pp. 249–284.
3. Sternberg, A.; Bardow, A. Life cycle assessment of Power-to-Gas: Syngas vs methane. *ACS Sustain. Chem. Eng.* **2016**, *4*, 4156–4165. [[CrossRef](#)]
4. Olah, G.A.; Goepfert, A.; Prakash, G.K.S. Chemical recycling of carbon dioxide to methanol and dimethyl ether: From greenhouse gas to renewable, environmentally carbon neutral fuels and synthetic hydrocarbons. *J. Org. Chem.* **2009**, *74*, 487–498. [[CrossRef](#)] [[PubMed](#)]
5. Niethammer, B.; Wodarz, S.; Betz, M.; Haltenort, P.; Oestreich, D.; Hackbarth, K.; Arnold, U.; Otto, T.; Sauer, J. Alternative liquid fuels from renewable resources. *Chem. Ing. Tech.* **2018**, *90*, 99–112. [[CrossRef](#)]
6. Zimmermann, M.C.; Otto, T.N.; Wodarz, S.; Zevaco, T.A.; Pitter, S. Mesoporous H-ZSM-5 for the conversion of dimethyl ether to hydrocarbons. *Chem. Ing. Tech.* **2019**, *91*, 1302–1313. [[CrossRef](#)]
7. Saravanan, K.; Ham, H.; Tsubaki, N.; Bae, J.W. Recent progress for direct synthesis of dimethyl ether from syngas on the heterogeneous bifunctional hybrid catalysts. *Appl. Catal. B* **2017**, *217*, 494–522. [[CrossRef](#)]
8. Peral, E.; Martín, M. Optimal production of dimethyl ether from Switchgrass-Based syngas via direct synthesis. *Ind. Eng. Chem. Res.* **2015**, *54*, 7465–7475. [[CrossRef](#)]
9. Arena, F.; Barbera, K.; Italiano, G.; Bonura, G.; Spadaro, L.; Frusteri, F. Synthesis, characterization and activity pattern of Cu–ZnO/ZrO<sub>2</sub> catalysts in the hydrogenation of carbon dioxide to methanol. *J. Catal.* **2007**, *249*, 185–194. [[CrossRef](#)]
10. Arena, F.; Italiano, G.; Barbera, K.; Bonura, G.; Spadaro, L.; Frusteri, F. Basic evidences for methanol-synthesis catalyst design. *Catal. Today* **2009**, *143*, 80–85. [[CrossRef](#)]
11. Arena, F.; Italiano, G.; Barbera, K.; Bordiga, S.; Bonura, G.; Spadaro, L.; Frusteri, F. Solid-state interactions, adsorption sites and functionality of Cu-ZnO/ZrO<sub>2</sub> catalysts in the CO<sub>2</sub> hydrogenation to CH<sub>3</sub>OH. *Appl. Catal. A* **2008**, *350*, 16–23. [[CrossRef](#)]
12. Bonura, G.; Cordaro, M.; Cannilla, C.; Arena, F.; Frusteri, F. The changing nature of the active site of Cu-Zn-Zr catalysts for the CO<sub>2</sub> hydrogenation reaction to methanol. *Appl. Catal. B* **2014**, *152–153*, 152–161. [[CrossRef](#)]
13. Chen, S.; Zhang, J.; Wang, P.; Wang, X.; Song, F.; Bai, Y.; Zhang, M.; Wu, Y.; Xie, H.; Tan, Y. Effect of Vapor-phase-treatment to CuZnZr Catalyst on the reaction behaviors in CO<sub>2</sub> hydrogenation into methanol. *ChemCatChem* **2019**, *11*, 1448–1457. [[CrossRef](#)]
14. Larmier, K.; Liao, W.C.; Tada, S.; Lam, E.; Verel, R.; Bansode, A.; Urakawa, A.; Comas-Vives, A.; Copéret, C. CO<sub>2</sub>-to-Methanol hydrogenation on zirconia-supported copper nanoparticles: Reaction intermediates and the role of the Metal-Support interface. *Angew. Chem. Int. Ed.* **2017**, *56*, 2318–2323. [[CrossRef](#)]
15. Samson, K.; Śliwa, M.; Socha, R.P.; Góra-Marek, K.; Mucha, D.; Rutkowska-Zbik, D.; Paul, J.F.; Ruggiero-Mikołajczyk, M.; Grabowski, R.; Słoczyński, J. Influence of ZrO<sub>2</sub> structure and copper electronic state on activity of Cu/ZrO<sub>2</sub> catalysts in methanol synthesis from CO<sub>2</sub>. *ACS Catal.* **2014**, *4*, 3730–3741. [[CrossRef](#)]
16. Tada, S.; Katagiri, A.; Kiyota, K.; Honma, T.; Kamei, H.; Nariyuki, A.; Uchida, S.; Satokawa, S. Cu species incorporated into amorphous ZrO<sub>2</sub> with high activity and selectivity in CO<sub>2</sub>-to-Methanol hydrogenation. *J. Phys. Chem. C* **2018**, *122*, 5430–5442. [[CrossRef](#)]

17. Tada, S.; Kayamori, S.; Honma, T.; Kamei, H.; Nariyuki, A.; Kon, K.; Toyao, T.; Shimizu, K.-i.; Satokawa, S. Design of interfacial sites between Cu and amorphous ZrO<sub>2</sub> dedicated to CO<sub>2</sub>-to-Methanol hydrogenation. *ACS Catal.* **2018**, *8*, 7809–7819. [[CrossRef](#)]
18. Tada, S.; Larmier, K.; Büchel, R.; Copéret, C. Methanol synthesis via CO<sub>2</sub> hydrogenation over CuO–ZrO<sub>2</sub> prepared by two-nozzle flame spray pyrolysis. *Catal. Sci. Technol.* **2018**, *8*, 2056–2060. [[CrossRef](#)]
19. Zhang, Y.; Zhong, L.; Wang, H.; Gao, P.; Li, X.; Xiao, S.; Ding, G.; Wei, W.; Sun, Y. Catalytic performance of spray-dried Cu/ZnO/Al<sub>2</sub>O<sub>3</sub>/ZrO<sub>2</sub> catalysts for slurry methanol synthesis from CO<sub>2</sub> hydrogenation. *J. CO<sub>2</sub> Util.* **2016**, *15*, 72–82. [[CrossRef](#)]
20. Scotti, N.; Bossola, F.; Zaccheria, F.; Ravasio, N. Copper–Zirconia catalysts: Powerful multifunctional catalytic tools to approach sustainable processes. *Catalysts* **2020**, *10*, 168. [[CrossRef](#)]
21. Hong, Q.-J.; Liu, Z.-P. Mechanism of CO<sub>2</sub> hydrogenation over Cu/ZrO<sub>2</sub>(212) interface from first-principles kinetics Monte Carlo simulations. *Surf. Sci.* **2010**, *604*, 1869–1876. [[CrossRef](#)]
22. Lam, E.; Larmier, K.; Wolf, P.; Tada, S.; Safonova, O.V.; Copéret, C. Isolated Zr surface sites on silica promote hydrogenation of CO<sub>2</sub> to CH<sub>3</sub>OH in supported Cu catalysts. *J. Am. Chem. Soc.* **2018**, *140*, 10530–10535. [[CrossRef](#)] [[PubMed](#)]
23. Wang, W.; Qu, Z.; Song, L.; Fu, Q. CO<sub>2</sub> hydrogenation to methanol over Cu/CeO<sub>2</sub> and Cu/ZrO<sub>2</sub> catalysts: Tuning methanol selectivity via metal-support interaction. *J. Energy Chem.* **2020**, *40*, 22–30. [[CrossRef](#)]
24. Tang, Q.-L.; Hong, Q.-J.; Liu, Z.-P. CO<sub>2</sub> fixation into methanol at Cu/ZrO<sub>2</sub> interface from first principles kinetic Monte Carlo. *J. Catal.* **2009**, *263*, 114–122. [[CrossRef](#)]
25. Polierer, S.; Jelic, J.; Pitter, S.; Studt, F. On the reactivity of the Cu/ZrO<sub>2</sub> system for the hydrogenation of CO<sub>2</sub> to methanol: A density functional theory study. *J. Phys. Chem. C* **2019**, *123*, 26904–26911. [[CrossRef](#)]
26. Behrens, M.; Brennecke, D.; Girgsdies, F.; Kifner, S.; Trunschke, A.; Nasrudin, N.; Zakaria, S.; Idris, N.F.; Hamid, S.B.A.; Knip, B.; et al. Understanding the complexity of a catalyst synthesis: Co-precipitation of mixed Cu,Zn,Al hydroxycarbonate precursors for Cu/ZnO/Al<sub>2</sub>O<sub>3</sub> catalysts investigated by titration experiments. *Appl. Catal. A* **2011**, *392*, 93–102. [[CrossRef](#)]
27. Bems, B.; Schur, M.; Dassenoy, A.; Junkes, H.; Herein, D.; Schlögl, R. Relations between synthesis and microstructural properties of copper/zinc hydroxycarbonates. *Chem. Eur. J.* **2003**, *9*, 2039–2052. [[CrossRef](#)]
28. Raudaskoski, R.; Niemelä, M.V.; Keiski, R.L. The effect of ageing time on co-precipitated Cu/ZnO/ZrO<sub>2</sub> catalysts used in methanol synthesis from CO<sub>2</sub> and H<sub>2</sub>. *Top. Catal.* **2007**, *45*, 57–60. [[CrossRef](#)]
29. Jung, K.T.; Bell, A.T. Effects of zirconia phase on the synthesis of methanol over zirconia-supported copper. *Catal. Lett.* **2002**, *80*, 63–68. [[CrossRef](#)]
30. Frusteri, F.; Cordaro, M.; Cannilla, C.; Bonura, G. Multifunctionality of Cu–ZnO–ZrO<sub>2</sub>/H-ZSM5 catalysts for the one-step CO<sub>2</sub>-to-DME hydrogenation reaction. *Appl. Catal. B* **2015**, *162*, 57–65. [[CrossRef](#)]
31. Ahmad, R.; Hellinger, M.; Buchholz, M.; Sezen, H.; Gharnati, L.; Wöll, C.; Sauer, J.; Döring, M.; Grunwaldt, J.-D.; Arnold, U. Flame-made Cu/ZnO/Al<sub>2</sub>O<sub>3</sub> catalyst for dimethyl ether production. *Catal. Commun.* **2014**, *43*, 52–56. [[CrossRef](#)]
32. Jiang, X.; Qin, X.; Ling, C.; Wang, Z.; Lu, J. The effect of mixing on Co-precipitation and evolution of microstructure of Cu–ZnO catalyst. *AIChE J.* **2018**, *64*, 2647–2654. [[CrossRef](#)]
33. Jiang, X.; Zheng, L.; Wang, Z.; Lu, J. Microstructure characters of Cu/ZnO catalyst precipitated inside microchannel reactor. *J. Mol. Catal. A Chem.* **2016**, *423*, 457–462. [[CrossRef](#)]
34. Kaluza, S.; Behrens, M.; Schiefenhövel, N.; Knip, B.; Fischer, R.; Schlögl, R.; Muhler, M. A Novel synthesis route for Cu/ZnO/Al<sub>2</sub>O<sub>3</sub> catalysts used in methanol synthesis: Combining continuous consecutive precipitation with continuous aging of the precipitate. *ChemCatChem* **2011**, *3*, 189–199. [[CrossRef](#)]
35. Simson, G.; Prasetyo, E.; Reiner, S.; Hinrichsen, O. Continuous precipitation of Cu/ZnO/Al<sub>2</sub>O<sub>3</sub> catalysts for methanol synthesis in microstructured reactors with alternative precipitating agents. *Appl. Catal. A* **2013**, *450*, 1–12. [[CrossRef](#)]
36. Zhang, Q.-C.; Cheng, K.-P.; Wen, L.-X.; Guo, K.; Chen, J.-F. A study on the precipitating and aging processes of CuO/ZnO/Al<sub>2</sub>O<sub>3</sub> catalysts synthesized in micro-impinging stream reactors. *RSC Adv.* **2016**, *6*, 33611–33621. [[CrossRef](#)]
37. Schur, M.; Bems, B.; Dassenoy, A.; Kassatkine, I.; Urban, J.; Wilmes, H.; Hinrichsen, O.; Muhler, M.; Schlögl, R. Continuous coprecipitation of catalysts in a micromixer: Nanostructured Cu/ZnO composite for the synthesis of methanol. *Angew. Chem. Int. Ed.* **2003**, *42*, 3815–3817. [[CrossRef](#)]

38. Angelo, L.; Girleanu, M.; Ersen, O.; Serra, C.; Parkhomenko, K.; Roger, A.-C. Catalyst synthesis by continuous coprecipitation under micro-fluidic conditions: Application to the preparation of catalysts for methanol synthesis from CO<sub>2</sub>/H<sub>2</sub>. *Catal. Today* **2016**, *270*, 59–67. [[CrossRef](#)]
39. Huang, C.; Mao, D.; Guo, X.; Yu, J. Microwave-assisted hydrothermal synthesis of CuO-ZnO-ZrO<sub>2</sub> as catalyst for direct synthesis of methanol by carbon dioxide hydrogenation. *Energy Technol.* **2017**, *5*, 2100–2107. [[CrossRef](#)]
40. Wolf, A.; Michele, V.; Schlüter, O.F.K.; Herbstritt, F.; Heck, J.; Mleczko, L. Precipitation in a Micromixer—From laboratory to industrial scale. *Chem. Eng. Technol.* **2015**, *38*, 2017–2024. [[CrossRef](#)]
41. Hartig, M.A.J.; Jacobsen, N.; Peukert, W. Multi-component and multi-phase population balance model: The case of Georgeite formation as methanol catalyst precursor phase. *Chem. Eng. Sci.* **2014**, *109*, 158–170. [[CrossRef](#)]
42. Behrens, M.; Schlögl, R. How to prepare a good Cu/ZnO catalyst or the role of solid state chemistry for the synthesis of nanostructured catalysts. *Z. Anorg. Allg. Chem.* **2013**, *639*, 2683–2695. [[CrossRef](#)]
43. Muhr, H.; David, R.; Villermaux, J. Crystallization and precipitation engineering -V. Simulation of the precipitation of silver bromide octahedral crystals in a double-jet semi-batch reactor. *Chem. Eng. Sci.* **1995**, *50*, 345–355. [[CrossRef](#)]
44. Rehage, H.; Scherer, S.; Kind, M. A steady-state precipitation model for flowsheet simulation and its application. *Comput. Chem. Eng.* **2019**, *128*, 524–537. [[CrossRef](#)]
45. Vicum, L.; Mazzotti, M. Multi-scale modeling of a mixing-precipitation process in a semibatch stirred tank. *Chem. Eng. Sci.* **2007**, *62*, 3513–3527. [[CrossRef](#)]
46. Ahmadi, F.; Haghighi, M.; Ajamein, H. Sonochemically coprecipitation synthesis of CuO/ZnO/ZrO<sub>2</sub>/Al<sub>2</sub>O<sub>3</sub> nanocatalyst for fuel cell grade hydrogen production via steam methanol reforming. *J. Mol. Catal. A Chem.* **2016**, *421*, 196–208. [[CrossRef](#)]
47. Allahyari, S.; Haghighi, M.; Ebadi, A.; Hosseinzadeh, S. Effect of irradiation power and time on ultrasound assisted co-precipitation of nanostructured CuO–ZnO–Al<sub>2</sub>O<sub>3</sub> over HZSM-5 used for direct conversion of syngas to DME as a green fuel. *Energy Convers. Manag.* **2014**, *83*, 212–222. [[CrossRef](#)]
48. Baldyga, J.; Bourne, J.R. *Turbulent Mixing and Chemical Reactions*; Wiley: Chichester, UK, 1999.
49. Metzger, L.; Kind, M. On the mixing in confined impinging jet mixers—Time scale analysis and scale-up using CFD coarse-graining methods. *Chem. Eng. Res. Des.* **2016**, *109*, 464–476. [[CrossRef](#)]
50. Rehage, H.; Nikq, F.; Kind, M. Experimental investigation of a two-zone model for semi-batch precipitation in stirred-tank reactors. *Chem. Eng. Sci.* **2019**, *207*, 258–270. [[CrossRef](#)]
51. Wei, H.; Zhou, W.; Garside, J. Computational fluid dynamics modeling of the precipitation process in a semibatch crystallizer. *Ind. Eng. Chem. Res.* **2001**, *40*, 5255–5261. [[CrossRef](#)]
52. Kügler, R.T.; Beißert, K.; Kind, M. On heterogeneous nucleation during the precipitation of barium sulfate. *Chem. Eng. Res. Des.* **2016**, *114*, 30–38. [[CrossRef](#)]
53. Kügler, R.T.; Kind, M. Experimental study about plugging in confined impinging jet mixers during the precipitation of strontium sulfate. *Chem. Eng. Process.* **2016**, *101*, 25–32. [[CrossRef](#)]
54. Schwarzer, H.-C.; Peukert, W. Combined experimental/numerical study on the precipitation of nanoparticles. *AIChE J.* **2004**, *50*, 3234–3247. [[CrossRef](#)]
55. Catizzzone, E.; Migliori, M.; Purita, A.; Giordano, G. Ferrierite vs.  $\gamma$ -Al<sub>2</sub>O<sub>3</sub>: The superiority of zeolites in terms of water-resistance in vapour-phase dehydration of methanol to dimethyl ether. *J. Energy Chem.* **2019**, *30*, 162–169. [[CrossRef](#)]
56. Frusteri, F.; Migliori, M.; Cannilla, C.; Frusteri, L.; Catizzzone, E.; Aloise, A.; Giordano, G.; Bonura, G. Direct CO<sub>2</sub>-to-DME hydrogenation reaction: New evidences of a superior behaviour of FER-based hybrid systems to obtain high DME yield. *J. CO<sub>2</sub> Util.* **2017**, *18*, 353–361. [[CrossRef](#)]
57. Migliori, M.; Aloise, A.; Catizzzone, E.; Giordano, G. Kinetic analysis of methanol to dimethyl ether reaction over H-MFI catalyst. *Ind. Eng. Chem. Res.* **2014**, *53*, 14885–14891. [[CrossRef](#)]
58. Stiefel, M.; Ahmad, R.; Arnold, U.; Döring, M. Direct synthesis of dimethyl ether from carbon-monoxide-rich synthesis gas: Influence of dehydration catalysts and operating conditions. *Fuel Process. Technol.* **2011**, *92*, 1466–1474. [[CrossRef](#)]
59. Tokay, K.C.; Dogu, T.; Dogu, G. Dimethyl ether synthesis over alumina based catalysts. *Chem. Eng. J.* **2012**, *184*, 278–285. [[CrossRef](#)]

60. Bae, J.W.; Kang, S.-H.; Lee, Y.-J.; Jun, K.-W. Synthesis of DME from syngas on the bifunctional Cu–ZnO–Al<sub>2</sub>O<sub>3</sub>/Zr-modified ferrierite: Effect of Zr content. *Appl. Catal. B* **2009**, *90*, 426–435. [[CrossRef](#)]
61. Bae, J.W.; Kang, S.-H.; Lee, Y.-J.; Jun, K.-W. Effect of precipitants during the preparation of Cu–ZnO–Al<sub>2</sub>O<sub>3</sub>/Zr-ferrierite catalyst on the DME synthesis from syngas. *J. Ind. Eng. Chem.* **2009**, *15*, 566–572. [[CrossRef](#)]
62. Bonura, G.; Cannilla, C.; Frusteri, L.; Frusteri, F. The influence of different promoter oxides on the functionality of hybrid CuZn-ferrierite systems for the production of DME from CO<sub>2</sub>-H<sub>2</sub> mixtures. *Appl. Catal. A* **2017**, *544*, 21–29. [[CrossRef](#)]
63. Bonura, G.; Cannilla, C.; Frusteri, L.; Mezzapica, A.; Frusteri, F. DME production by CO<sub>2</sub> hydrogenation: Key factors affecting the behaviour of CuZnZr/ferrierite catalysts. *Catal. Today* **2017**, *281*, 337–344. [[CrossRef](#)]
64. Catizzone, E.; Daele, S.V.; Bianco, M.; Di Michele, A.; Aloise, A.; Migliori, M.; Valtchev, V.; Giordano, G. Catalytic application of ferrierite nanocrystals in vapour-phase dehydration of methanol to dimethyl ether. *Appl. Catal. B* **2019**, *243*, 273–282. [[CrossRef](#)]
65. Lee, Y.J.; Jung, M.H.; Lee, J.-B.; Jeong, K.-E.; Roh, H.-S.; Suh, Y.-W.; Bae, J.W. Single-step synthesis of dimethyl ether from syngas on Al<sub>2</sub>O<sub>3</sub>-modified CuO–ZnO–Al<sub>2</sub>O<sub>3</sub>/ferrierite catalysts: Effects of Al<sub>2</sub>O<sub>3</sub> content. *Catal. Today* **2014**, *228*, 175–182. [[CrossRef](#)]
66. Roman-Leshkov, Y.; Moliner, M.; Davis, M.E. Impact of controlling the site distribution of Al atoms on catalytic properties in Ferrierite-Type zeolites. *J. Phys. Chem. C* **2011**, *115*, 1096–1102. [[CrossRef](#)]
67. Sai Prasad, P.S.; Bae, J.W.; Kang, S.-H.; Lee, Y.-J.; Jun, K.-W. Single-step synthesis of DME from syngas on Cu–ZnO–Al<sub>2</sub>O<sub>3</sub>/zeolite bifunctional catalysts: The superiority of ferrierite over the other zeolites. *Fuel Process. Technol.* **2008**, *89*, 1281–1286. [[CrossRef](#)]
68. Wu, J.; Luo, S.; Toyir, J.; Saito, M.; Takeuchi, M.; Watanabe, T. Optimization of preparation conditions and improvement of stability of Cu/ZnO-based multicomponent catalysts for methanol synthesis from CO<sub>2</sub> and H<sub>2</sub>. *Catal. Today* **1998**, *45*, 215–220. [[CrossRef](#)]
69. Frei, E.; Schaadt, A.; Ludwig, T.; Hillebrecht, H.; Krossing, I. The influence of the precipitation/ageing temperature on a Cu/ZnO/ZrO<sub>2</sub> catalyst for methanol synthesis from H<sub>2</sub> and CO<sub>2</sub>. *ChemCatChem* **2014**, *6*, 1721–1730. [[CrossRef](#)]
70. Ruland, H.; Song, H.; Laudenschleger, D.; Stürmer, S.; Schmidt, S.; He, J.; Kähler, K.; Muhler, M.; Schlögl, R. CO<sub>2</sub> hydrogenation with Cu/ZnO/Al<sub>2</sub>O<sub>3</sub>: A benchmark study. *ChemCatChem* **2020**, *12*, 1–8. [[CrossRef](#)]
71. Dadgar, F.; Myrstad, R.; Pfeifer, P.; Holmen, A.; Venvik, H.J. Direct dimethyl ether synthesis from synthesis gas: The influence of methanol dehydration on methanol synthesis reaction. *Catal. Today* **2016**, *270*, 76–84. [[CrossRef](#)]
72. Chanchlani, K.G.; Hudgins, R.R.; Silveston, P.L. Methanol synthesis from H<sub>2</sub>, CO, and CO<sub>2</sub> over Cu/ZnO catalysts. *J. Catal.* **1992**, *136*, 59–75. [[CrossRef](#)]
73. Liu, G.; Willcox, G.; Garland, M.; Kung, H.H. The rate of methanol production on a Copper-Zinc oxide catalyst: The dependence on the feed composition. *J. Catal.* **1984**, *90*, 139–146. [[CrossRef](#)]
74. Studt, F.; Behrens, M.; Kunkes, E.L.; Thomas, N.; Zander, S.; Tarasov, A.; Schumann, J.; Frei, E.; Varley, J.B.; Abild-Pedersen, F.; et al. The mechanism of CO and CO<sub>2</sub> hydrogenation to methanol over Cu-Based catalysts. *ChemCatChem* **2015**, *7*, 1105–1111. [[CrossRef](#)]
75. Jones, A.J.; Carr, R.T.; Zones, S.I.; Iglesia, E. Acid strength and solvation in catalysis by MFI zeolites and effects of the identity, concentration and location of framework heteroatoms. *J. Catal.* **2014**, *312*, 58–68. [[CrossRef](#)]
76. Baltés, C.; Vukojevic, S.; Schüth, F. Correlations between synthesis, precursor, and catalyst structure and activity of a large set of CuO/ZnO/Al<sub>2</sub>O<sub>3</sub> catalysts for methanol synthesis. *J. Catal.* **2008**, *258*, 334–344. [[CrossRef](#)]
77. Behrens, M. Coprecipitation: An excellent tool for the synthesis of supported metal catalysts—From the understanding of the well known recipes to new materials. *Catal. Today* **2015**, *246*, 46–54. [[CrossRef](#)]
78. Behrens, M.; Studt, F.; Kasatkin, I.; Kühl, S.; Hävecker, M.; Abild-Pedersen, F.; Zander, S.; Girgsdies, F.; Kurr, P.; Knief, B.-L.; et al. The active site of methanol synthesis over Cu/ZnO/Al<sub>2</sub>O<sub>3</sub> industrial catalysts. *Science* **2012**, *336*, 893–897. [[CrossRef](#)]
79. Kurtz, M.; Bauer, N.; Büscher, C.; Wilmer, H.; Hinrichsen, O.; Becker, R.; Rabe, S.; Merz, K.; Driess, M.; Fischer, R.A.; et al. New synthetic routes to more active Cu/ZnO catalysts used for methanol synthesis. *Catal. Lett.* **2004**, *92*, 49–52. [[CrossRef](#)]

80. Kügler, R.T.; Doyle, S.; Kind, M. Fundamental insights into barium sulfate precipitation by time-resolved in situ synchrotron radiation wide-angle X-ray scattering (WAXS). *Chem. Eng. Sci.* **2015**, *133*, 140–147. [[CrossRef](#)]
81. Kügler, R.T.; Kind, M. On precipitation of sparingly soluble fluoride salts. *Cryst. Growth Des.* **2018**, *18*, 728–733. [[CrossRef](#)]
82. Spencer, M.S. Precursors of copper/zinc oxide catalysts. *Catal. Lett.* **2000**, *66*, 255–257. [[CrossRef](#)]
83. Thommes, M.; Kaneko, K.; Neimark, A.V.; Olivier, J.P.; Rodriguez-Reinoso, F.; Rouquerol, J.; Sing, K.S.W. Physisorption of gases, with special reference to the evaluation of surface area and pore size distribution (IUPAC Technical Report). *Pure Appl. Chem.* **2015**, *87*, 1051–1069. [[CrossRef](#)]
84. Brunauer, S.; Emmet, P.H.; Teller, E. Adsorption of gases in multimolecular layers. *J. Am. Chem. Soc.* **1938**, *60*, 309–319. [[CrossRef](#)]
85. Barrett, E.P.; Joyner, L.G.; Halenda, P.P. The determination of pore volume and area distributions in porous substances. i. computations from nitrogen isotherms. *J. Am. Chem. Soc.* **1951**, *73*, 373–380. [[CrossRef](#)]
86. Hinrichsen, O.; Genger, T.; Muhler, M. Chemisorption of N<sub>2</sub>O and H<sub>2</sub> for the surface determination of copper catalysts. *Chem. Eng. Technol.* **2000**, *23*, 956–959. [[CrossRef](#)]



© 2020 by the authors. Licensee MDPI, Basel, Switzerland. This article is an open access article distributed under the terms and conditions of the Creative Commons Attribution (CC BY) license (<http://creativecommons.org/licenses/by/4.0/>).